

# Mapping metals at high redshift with far-infrared lines

A. Pallottini<sup>1\*</sup>, S. Gallerani<sup>1</sup>, A. Ferrara<sup>1,2</sup>, B. Yue<sup>1</sup>, L. Vallini<sup>3</sup>, R. Maiolino<sup>4</sup>,  
& C. Feruglio<sup>1,5</sup>

<sup>1</sup>*Scuola Normale Superiore, Piazza dei Cavalieri 7, I-56126 Pisa, Italy*

<sup>2</sup>*Kavli IPMU, The University of Tokyo, 5-1-5 Kashiwanoha, Kashiwa 277-8583, Japan*

<sup>3</sup>*Dipartimento di Fisica e Astronomia, Università di Bologna, viale Berti Pichat 6/2, 40127 Bologna, Italy*

<sup>4</sup>*Cavendish Laboratory, University of Cambridge, 19 J. J. Thomson Ave., Cambridge CB3 0HE, UK*

<sup>5</sup>*INAF, Osservatorio Astronomico di Roma, Via Frascati 33, 00040 Monteporzio Catone, Italy*

## ABSTRACT

Cosmic metal enrichment is one of the key physical processes regulating galaxy formation and the evolution of the intergalactic medium (IGM). However, determining the metal content of the most distant galaxies has proven so far almost impossible; also, absorption line experiments at  $z \gtrsim 6$  become increasingly difficult because of instrumental limitations and the paucity of background quasars. With the advent of ALMA, far-infrared emission lines provide a novel tool to study early metal enrichment. Among these, the [C II] line at  $157.74 \mu\text{m}$  is the most luminous line emitted by the interstellar medium of galaxies. It can also resonant scatter CMB photons inducing characteristic intensity fluctuations ( $\Delta I/I_{\text{CMB}}$ ) near the peak of the CMB spectrum, thus allowing to probe the low-density IGM. We compute both [C II] galaxy emission and metal-induced CMB fluctuations at  $z \sim 6$  by using Adaptive Mesh Refinement cosmological hydrodynamical simulations and produce mock observations to be directly compared with ALMA BAND6 data ( $\nu_{\text{obs}} \sim 272 \text{ GHz}$ ). The [C II] line flux is correlated with  $M_{\text{UV}}$  as  $\log(F_{\text{peak}}/\mu\text{Jy}) = -27.205 - 2.253 M_{\text{UV}} - 0.038 M_{\text{UV}}^2$ . Such relation is in very good agreement with recent ALMA observations (e.g. Maiolino et al. 2015; Capak et al. 2015) of  $M_{\text{UV}} < -20$  galaxies. We predict that a  $M_{\text{UV}} = -19$  ( $M_{\text{UV}} = -18$ ) galaxy can be detected at  $4\sigma$  in  $\simeq 40$  (2000) hours, respectively. CMB resonant scattering can produce  $\simeq \pm 0.1 \mu\text{Jy}/\text{beam}$  emission/absorptions features that are very challenging to be detected with current facilities. The best strategy to detect these signals consists in the stacking of deep ALMA observations pointing fields with known  $M_{\text{UV}} \simeq -19$  galaxies. This would allow to simultaneously detect both [C II] emission from galactic reionization sources and CMB fluctuations produced by  $z \sim 6$  metals.

**Key words:** cosmology: cosmic microwave background – infrared: general – galaxies: high-redshift – galaxies: intergalactic medium

## 1 INTRODUCTION

In  $\Lambda\text{CDM}$  cosmologies<sup>1</sup>, structure formation is a hierarchical bottom-up process (i.e. Press & Schechter 1974). Dwarf galaxies are expected to be abundant and to represent the first ( $z \gtrsim 10$ ) efficient metal factories of the Universe (e.g. Madau et al. 2001; Ferrara 2008). These galaxies effectively pollute their surrounding intergalactic medium (IGM), since

– compared to larger galaxies – dwarfs have a shallower potential well and because their smaller size allows multiple SN to coherently drive the outflows (e.g. Ferrara & Tolstoy 2000).

In spite of the impressive progresses produced by deep optical/IR surveys (Dunlop 2013; Madau & Dickinson 2014; Bouwens et al. 2014) in identifying galaxies well within the Epoch of Reionization, very little is known about the metallicity and other properties of these systems, including feedback (e.g. Dayal et al. 2014) and interactions with their environment (e.g. Barnes et al. 2014).

The situation is slightly better for what concerns the IGM, where metal enrichment is typically studied by measuring the abundance of heavy elements at different cosmic times with quasar (QSO) absorption line spectroscopy (e.g.

\* email: andrea.pallottini@sns.it

<sup>1</sup> In this work we assume a  $\Lambda\text{CDM}$  cosmology with total matter, vacuum and baryonic densities in units of the critical density  $\Omega_{\Lambda} = 0.727$ ,  $\Omega_{dm} = 0.228$ ,  $\Omega_b = 0.045$ , Hubble constant  $H_0 = 100 \text{ h km s}^{-1} \text{ Mpc}^{-1}$  with  $h = 0.704$ , spectral index  $n = 0.967$ ,  $\sigma_8 = 0.811$  (Larson et al. 2011).

Songaila 2005; Ryan-Weber et al. 2009; Becker et al. 2009; Simcoe et al. 2011; D’Odorico et al. 2013) and – more recently – with gamma-ray bursts soft X-ray absorption (e.g. Campana et al. 2010; Behar et al. 2011; Campana et al. 2015). These observations show that the diffuse IGM is enriched at metallicity  $Z \gtrsim 10^{-3.5} Z_{\odot}$  at any overdensity ( $\Delta$ ) and redshift ( $z$ ) probed so far (Meiksin 2009). As the gas left over by the Big Bang is (virtually) metal-free, understanding how and when the first metals were produced holds the key of many structure formation processes.

As a consequence of the paucity of standard luminous lighthouses prior to reionization (Barkana & Loeb 2001; Ciardi & Ferrara 2005), the enrichment at  $z \gtrsim 6$  cannot be efficiently studied with absorption line experiments. Additionally, at high- $z$  the detection of most metal tracers becomes increasingly difficult. For example, C IV metal absorption line detections at high- $z$  are rare since the C IV doublet shifts into the near-infrared. In this spectral regions observations become challenging because of increased OH emission from the sky and severe telluric absorption.

The above situation is going to change very soon thanks to the advent of the Atacama Large Millimeter-submillimeter Array (ALMA). This observatory gives us access to far-infrared (FIR) and sub-mm spectroscopy, where metal lines carrying information about the energetics of the interstellar medium and outflows are found. FIR emission lines are a powerful tool to study high- $z$  galaxies, since – unlike Ly $\alpha$  – they are affected neither by the increasing IGM neutral fraction at  $z \gtrsim 6$  nor by the presence of dust.

In particular, the [C II] ( $^2P_{3/2} \rightarrow ^2P_{1/2}$ ) line at  $157.74 \mu\text{m}$  is the brightest FIR emission line, i.e. it can account for  $\sim 1\%$  of the total infrared luminosity of galaxies (e.g. Crawford et al. 1985; Madden et al. 1997). Before the advent of ALMA, [C II] observations at  $z \gtrsim 4$  were limited to QSO host galaxies and to rare galaxies with extreme star formation ( $\simeq 10^3 M_{\odot} \text{yr}^{-1}$ ) (e.g. Maiolino et al. 2005; Carilli & Walter 2013; Gallerani et al. 2012; Ciccone et al. 2015). The unprecedented resolution and sensitivity of ALMA offer the unique opportunity to search for [C II] emission from normal star forming galaxies ( $\simeq 1 - 10 M_{\odot} \text{yr}^{-1}$ ) at high- $z$  (e.g. Maiolino et al. 2015; Capak et al. 2015). These observations yield key information about the stellar age, gas metallicity, star formation, and also on the environments in which these early galaxies formed (e.g. González-López et al. 2014; De Looze et al. 2014). Recently, the [C II] emission arising from high- $z$  star forming galaxies has been modelled through numerical simulations (e.g. Nagamine et al. 2006; Vallini et al. 2013; Tomassetti et al. 2015; Vallini et al. 2015) and analytical models (e.g. Gong et al. 2012; Muñoz & Furlanetto 2014).

In addition to tracing the ISM of galaxies, FIR resonant lines correspond to transitions that are excited via a resonant scattering process of Cosmic Microwave Background (CMB) photons on heavy element atoms present in the IGM (e.g. de Bernardis et al. 1993; Maoli et al. 1996). These resonant transitions are available for essentially all the most abundant species, e.g. C, N, O, Si, S and Fe, in the mid-IR and FIR wavelength ranges (e.g. Basu et al. 2004).

As a result, IGM metals can produce CMB spectral distortions and spatial fluctuations that can be used to extract unique information on the cosmic metal enrichment process, like, for example, spatial distribution maps of a given metal

species. This experiment is conceptually similar to QSO absorption line studies, but it uses the CMB as a background source: the method has the enormous advantage that every pixel in a sky map can act as a source against which metal lines may appear either in emission or absorption.

Various works (e.g. Maoli et al. 2005; Basu 2007; Schleicher et al. 2008) have proposed CMB fluctuations/distortions as a tool to trace the smooth distribution of metals and molecules in the post-recombination Universe ( $z \gg 10$ ). These fluctuations typically affect the first CMB multipoles – at  $l \lesssim 10^2$ , large angular scales ( $\theta \sim 1 \text{ deg}$ ) – and they will be hopefully seen by *Planck* successors (e.g. Hernández-Monteagudo et al. 2006; Chluba 2014). On smaller scales –  $\theta \sim 10''$  ( $l \gtrsim 10^5$ ) – CMB fluctuations in the FIR can be used to map the enriched IGM surrounding the first galaxies ( $z \gtrsim 10$ ).

Here we present a model based on detailed Adaptive Mesh Refinement hydrodynamical cosmological simulations, that allows us to simultaneously compute both the [C II] line emission from early galaxies and the expected level and statistical properties of CMB fluctuations arising from intergalactic C II resonant scattering.

The paper is organized as follows. In Sec. 2, we describe our model, introducing the adopted high- $z$  cosmic metal enrichment simulation (Sec. 2.1). We postprocess the simulation to account for [C II] galaxy emission (Sec. 2.2) and CMB fluctuations (Sec. 2.3), and analyze the properties of the simulated CMB fluctuations in Sec. 3. Then, we construct and analyze mock ALMA observations of [C II] galaxy emission and CMB fluctuations (Sec. 4). Finally, we propose and discuss an observational strategy for the detection of [C II] galaxy emission and metal-induced CMB fluctuations (Sec. 5). Conclusions are given in Sec. 6.

## 2 MODEL

### 2.1 Cosmological simulations

We start from the suite of cosmological hydrodynamical metal enrichment simulations presented by Pallottini et al. (2014a, P14 hereafter). Using a customized version of the Adaptive Mesh Refinement code RAMSES (Teyssier 2002), P14 follows the evolution of a  $(10 \text{ Mpc } h^{-1})^3$  comoving cosmic volume from  $z = 199$  until  $z = 4$  with  $512^3$  dark matter particles. The gas evolution is tracked on a corresponding number of coarse grid cells, with 4 additional levels of refinement based on a Lagrangian mass threshold-based criterion. This set-up allows us to reach a maximum resolution of  $1.22 h^{-1} \text{ kpc}$  for the gas in the densest regions.

Star formation and supernova feedback are included via customized subgrid prescriptions; P14 accounts for stellar yields based on population synthesized models (Salvadori et al. 2008). The simulated galaxy sample reproduces the observed cosmic star formation rate (Bouwens et al. 2012; Zheng et al. 2012) and stellar mass densities (González et al. 2011) evolution in the full redshift range  $4 \leq z \lesssim 10$ .

In P14, we track the progressive metal enrichment of the gas, initially of primordial (BBN) composition, and its thermal history by accounting for heating and cooling processes (Theuns et al. 1998). The gas ionization state is regulated by an external, redshift-dependent ionizing UV background

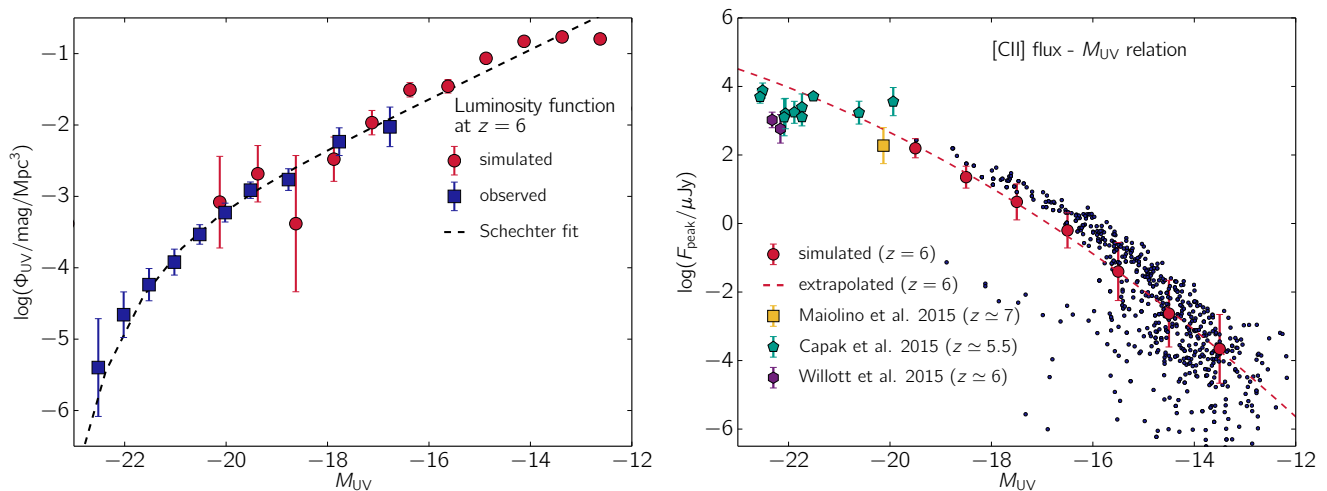


**Figure 1.** **Left panel:** UV luminosity function,  $\Phi_{UV}$  at  $z = 6$ . Red circles represent the simulated  $\Phi_{UV}$ ; blue squares denote the observed  $\Phi_{UV}$ , inferred from a composite collection of HST datasets (Bouwens et al. 2014); black dashed lines are the Schechter fit (Bouwens et al. 2014) to the observations. **Right panel:** [C II] flux as a function of  $M_{UV}$  at  $z = 6$  (blue small circles); the same relation binned in  $\Delta M_{UV} = 1$  intervals is shown by red circles. The red errorbars correspond to the r.m.s. variance within the magnitude intervals; The red dashed line is the best fit to the relation. Also plotted are the data from recent high- $z$  observations from Maiolino et al. (2015); Capak et al. (2015); Willott et al. (2015) with yellow squares, green pentagons and violet hexagons, respectively.

(Haardt & Madau 1996, 2012, UVB) produced both by stars and QSOs. At  $z \approx 6$ , the observationally allowed range for the UV photoionization rate is  $\approx (0.9 - 3.6) \times 10^{-13} \text{s}^{-1}$  (e.g. Wyithe & Bolton 2011). We have verified that the gas thermodynamical evolution is only marginally affected by UVB intensity variations within this range.

To compute the ionization state of the various atomic species, we postprocess the simulation outputs using the photoionization code CLOUDY (Ferland et al. 1998). Similar to P14, we account both for the UVB intensity at 912 Å ( $J_\nu$ ), and the density ( $n$ ), kinetic temperature ( $T_k$ ), and metallicity ( $Z$ ) of the gas.

We adopt the following classification for the baryonic gas: (i) the interstellar medium (ISM) defines highly over-dense gas ( $n/n_{\text{mean}} = \Delta \geq 10^3$ ); (ii) the *true* intergalactic medium (IGM) is characterized by  $\Delta \leq 10$ ; (iii) the circumgalactic medium (CGM) represents the interface between the IGM and ISM ( $10 < \Delta < 10^3$ ). Pallottini et al. (2014b) have shown that the adopted classification is consistent with the one proposed by Shull (2014), based on the distance  $r$  between the gas and the center of the galaxy. Specifically (i) the ISM is located within the galaxy virial radius ( $r_{\text{vir}}$ ), (ii) the IGM at  $r/r_{\text{vir}} \gtrsim 5$  and (iii) the CGM at  $1 \lesssim r/r_{\text{vir}} \lesssim 5$ .

In P14, we showed that galaxies develop a stellar mass-metallicity ( $M_\star - Z_\star$ ) relation by  $z = 6$ . For  $M_\star > 10^7 M_\odot$ , the stellar metallicity ( $Z_\star$ ) increases with increasing stellar mass, while for  $M_\star \lesssim 10^7 M_\odot$ ,  $Z_\star$  is constant. This means that, while massive galaxies are able to retain most of their metals, low mass galaxies are prone to metal ejection because of their shallower potential well. This indicates that at high- $z$  low mass galaxies are the main driver of metal enrichment in the IGM (e.g. Ferrara 2008). In agreement with previous numerical studies (e.g. Dayal et al. 2013), the  $M_\star - Z_\star$  relation shows little evolution from  $z = 6$  to  $z = 4$ , for galaxies with  $M_\star \approx 10^7$ . Our results are consistent with the metallicity evolution suggested by recent observations of  $3 < z < 5$  star forming galaxies (Troncoso et al. 2014).

We find that (i) most of the gas resides in the IGM, (ii) the denser CGM contains about 15% of the baryons and (iii) the ISM accounts only for a small fraction of the total mass ( $\approx 7\%$ ). On the other hand, at any given redshift the enriched gas is mostly found near the metal production site, i.e. in the ISM; less than 10% in mass of the produced metals can reach the IGM/CGM. In particular, at  $z = 4$ , a  $\Delta - Z$  relation is in place: the IGM shows a uniform distribution around  $Z \approx 10^{-3.5} Z_\odot$ , in the CGM  $Z$  steeply rises with  $\Delta$  up to  $10^{-2} Z_\odot$  and the ISM has  $Z \approx 10^{-1} Z_\odot$ . A considerable fraction ( $\gtrsim 50\%$ ) of the enriched IGM/CGM is in a hot state ( $T_k \gtrsim 10^{4.5} \text{K}$ ), meaning that most of the carbon is in C IV. Our analysis shows that C IV absorption line experiments can only probe  $\approx 2\%$  of the total produced carbon.

P14 results are in agreement with previous numerical studies in terms of the baryon thermodynamical state (e.g. Rasera & Teyssier 2006; Cen & Chisari 2011), the evolution of the metal filling factor (e.g. Oppenheimer et al. 2009; Johnson et al. 2013) and the  $\Delta - Z$  relation (e.g. Gnedin & Ostriker 1997; Oppenheimer et al. 2012). Additionally, the preliminary analysis of synthetic spectra extracted from the simulation is consistent with recent observations of metal absorption lines (D’Odorico et al. 2013).

As a further consistency check, we test the UV luminosity function ( $\Phi_{UV}$ ) extracted from the P14 simulation against observations of  $z = 6$  galaxies. For each galaxy in our simulation,  $M_{UV}$  is calculated with STARBURST99 (Leitherer et al. 2010), using  $Z_\star$  and the stellar age as input parameters. In the left panel of Fig. 1, we plot the simulated and observed  $\Phi_{UV}$  with red circles and blue squares, respectively. The observations are taken from a composite collection of HST datasets (Bouwens et al. 2014), and we additionally plot the Schechter fit to the observations with a black dashed line. The simulated  $\Phi_{UV}$  well matches the observed UV luminosity function for  $-20 \lesssim M_{UV} \lesssim -16$ . Additionally, the simulated  $\Phi_{UV}$  is in fair agreement with the Schechter fit

extrapolated at  $-16 \lesssim M_{\text{UV}} \lesssim -12$ . Note that, for the simulated  $\Phi_{\text{UV}}$ , the bright end is around  $M_{\text{UV}} \sim -19$ , where the large scatter is due to the limited simulated volume.

## 2.2 [C II] emission from the ISM of high- $z$ galaxies

Starting from the P14 simulations, we compute the [C II] emission at  $157.74 \mu\text{m}$  due to the  $^2P_{3/2} \rightarrow ^2P_{1/2}$  forbidden transition of ionized carbon in the ISM of galaxies. The [C II] line is the dominant coolant of the galaxy interstellar medium, and it can be collisionally excited under conditions present in different ISM phases, e.g. in the cold and warm neutral medium (CNM, WNM), in high density photodissociation regions (PDRs), and even in the ionized gas (Tielens & Hollenbach 1985; Wolfire et al. 1995, 2003; Abel 2006; Vallini et al. 2013).

In our cosmological hydrodynamic simulations, we cannot resolve sub-kpc scales, that are typical for different ISM structures (CNM, WNM and PDRs). To overcome this problem, we account for [C II] emission<sup>2</sup> from the ISM of high- $z$  galaxies by adopting the model presented in Vallini et al. (2013) and updated in Vallini et al. (2015) (V15 hereafter). V15 predicts the [C II] emission from CNM, WNM and PDRs within individual galaxies as a function of their metallicity ( $Z_*$ ) and star formation rate (SFR). The V15 model is based on the radiative transfer simulation of a high- $z$  galaxy; it includes a subgrid treatment for computing the thermodynamical equilibrium of the diffuse neutral medium (on  $\simeq 60 \text{ pc}$  scales); it allows to localize molecular clouds within the galaxy (on  $\simeq 1 - 10 \text{ pc}$  scales) and to compute the corresponding [C II] emission by means of the PDR code UCLPDR (Bell et al. 2005).

According to the V15 model<sup>3</sup>, the [C II] galaxy luminosity ( $L_{\text{CII}}$ ) depends on the galaxy SFR and metallicity through the following fitting formula:

$$\log(L_{\text{CII}}) = 7.0 + 1.2 \log(\text{SFR}) + 0.021 \log(Z_*) + 0.012 \log(\text{SFR}) \log(Z_*) - 0.74 \log^2(Z_*), \quad (1)$$

where  $L_{\text{CII}}$ , SFR and  $Z_*$  are in units of  $L_\odot$ ,  $M_\odot \text{ yr}^{-1}$  and  $Z_\odot$ , respectively. The V15 model has been used to interpret high- $z$  LAEs and LBGs [C II] observations (e.g. González-López et al. 2014; Ota et al. 2014), and V15 provides predictions consistent with [C II] observations of local metal-poor dwarf galaxies (De Looze et al. 2014). We compare the V15 predictions with the work by Muñoz & Furlanetto (2014) (see their eq. 8): for a  $\text{SFR} = 10^2 M_\odot/\text{yr}$  and a solar metallicity, according to the V15 model  $L_{\text{CII}} \simeq 2.5 \times 10^9 L_\odot$ , that is a factor  $\simeq 5$  higher than the one predicted by Muñoz & Furlanetto (2014), i.e.  $L_{\text{CII}} \simeq 5 \times 10^8 L_\odot$ . Given the uncertainties

<sup>2</sup> In the present work, we focus on [C II] emission from  $z \simeq 6$  galaxies. However, we note that the V15 model can be readily extended to compute the emission of fine structure lines from other heavy elements, such as, e.g. [N II] at  $122 \mu\text{m}$  and [O I] at  $63 \mu\text{m}$  (Vallini et al. 2013).

<sup>3</sup> The V15 model assumes that H II regions provide only a negligible contribution to the [C II] emission (González-López et al. 2014, in particular see Fig. 8). However, the relative fraction of [C II] emission arising from H II regions is not clearly known. As an indicative value, Vasta et al. (2010) observe a median contribution of  $\simeq 30\%$ . For a more detailed discussion, we address the interested reader to Yue et al. (2015).

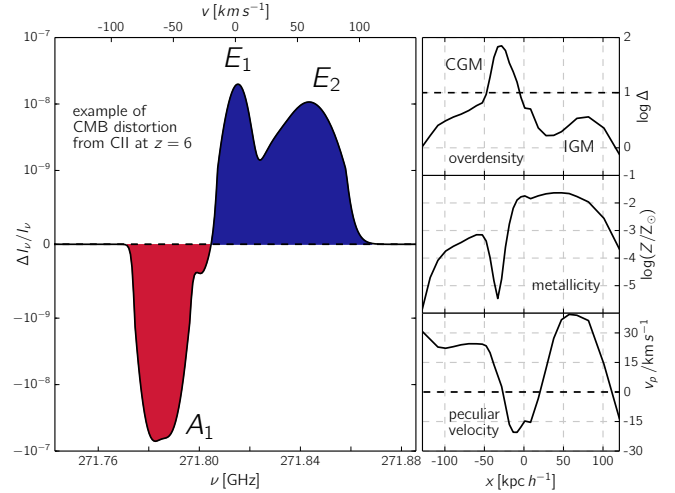


**Figure 2.** [C II] CMB spectral distortions/fluctuations from a simulated line of sight (l.o.s.) at  $z = 6$ . **Left panel:** intensity fluctuations ( $\Delta I_\nu/I_\nu$ ) as a function of frequency ( $\nu$ , lower axis) and velocity ( $v$ , upper axis). Absorption and emission features are highlighted in red and blue, respectively, and the corresponding peaks are labelled with  $A_i$  and  $E_i$ . Note that integration in the shown bandwidth ( $\Delta\nu \simeq 0.1 \text{ GHz}$ ) yields  $\Delta I/I \simeq -7 \times 10^{-7}$ . **Right panel:** overdensity ( $\Delta$ , top), metallicity ( $Z$ , center) and peculiar velocity ( $v_p$ , bottom) for the [C II] metal patch responsible for the fluctuations ( $|\Delta I_\nu/I_\nu| > 0$ ) as a function of co-moving distance ( $\text{kpc } h^{-1}$ ). In the overdensity plot our  $\Delta$  based IGM/CGM definition is marked with a dashed black line. In the peculiar velocity plot  $v_p = 0$  is marked with a dashed black line. The origins of both the velocity (left panel) and distance (right panel) axis are shifted for displaying purpose.

on the local [C II]-SFR relation,  $6 \times 10^8 \lesssim L_{\text{CII}}/L_\odot \lesssim 10^{10}$ , we find that both models are consistent with observations, though the V15 predictions provide a better match. To compute  $L_{\text{CII}}$  for galaxies in the P14 simulation we use eq. 1, where  $Z_*$  and SFR are the mass-averaged values derived from the simulation (see also Yue et al. 2015).

We calculate the relation between [C II] and UV emission. In the right panel of Fig. 1, we show the [C II] flux as a function of  $M_{\text{UV}}$  for the simulated galaxies at  $z = 6$  and for various  $z = 5 - 7$  ALMA observations (Maiolino et al. 2015; Capak et al. 2015; Willott et al. 2015). The simulated relation is shown as a scatter plot, binned in  $\Delta M_{\text{UV}} = 1$  intervals. The plot shows a clear correlation between [C II] flux and UV magnitude for the simulated galaxies, with a Spearman correlation coefficient of  $\simeq -0.78$ . The best fit formula for the relation is

$$\log(F_{\text{peak}}/\mu\text{Jy}) = -27.205 - 2.253 M_{\text{UV}} - 0.038 M_{\text{UV}}^2. \quad (2)$$

Using eq. 2 we can slightly extrapolate the simulated relation to  $M_{\text{UV}} < -20$ , and directly compare it with recent ALMA observations (right panel of Fig. 1), i.e. a [C II] detection in a  $z \simeq 7$  LBG (Maiolino et al. 2015, yellow square), observations of several “normal” ( $\sim L_*$ ) galaxies at  $z \simeq 5-6$  (Capak et al. 2015, green pentagons) and 2 LBGs at  $z \simeq 6$  (Willott et al. 2015, violet hexagons). Our model is in good agreement with the observations and local determinations ( $z \simeq 0$ ) of the  $L_{\text{CII}}$ -SFR relation (De Looze et al. 2014), as we discuss in more details in Sec. 5. For simulated galaxies



brighter than  $M_{\text{UV}} < -16$ , the  $F_{\text{peak}} - M_{\text{UV}}$  relation shows a bimodal trend: while 90% of the galaxies follow eq. 2, the remaining  $\simeq 10\%$  have fainter fluxes as a consequence of their lower metallicity values (see eq. 1).

We finally note that we limit our comparison between simulation results and observational data to  $z \simeq 6$  normal star forming galaxies ( $\text{SFR} \lesssim 10^2$ ) without considering [C II] observations in  $z \simeq 6$  QSO. In the latter case, observations refer to galaxies hosting super massive black holes ( $M_{\bullet} \sim 10^9 M_{\odot}$ ) that are not present in the P14 simulation, because of its limited volume.

### 2.3 CMB scattering from intergalactic metals

The IGM and CGM are not seen in emission, since their typical densities are too low ( $n < 0.1 \text{ cm}^{-3}$ ) for the upper levels of the [C II] transition to be efficiently populated through collisions with electrons and/or protons (Suginohara et al. 1999; Gong et al. 2012). In this case the spin temperature of the transition approaches the CMB one<sup>4</sup>.

As a result a C II ion at rest with respect to the CMB cannot show up in emission or absorption against this background (e.g. de Bernardis et al. 1993; Maoli et al. 1996; da Cunha et al. 2013). However, if the ion has a peculiar velocity, for example approaching with a velocity  $v_p$ , it will receive a larger (i.e. Doppler-boosted) CMB photon flux in the direction of its motion. As CMB photons are resonantly scattered (e.g. Basu et al. 2004; Basu 2007; Schleicher et al. 2008) by an atomic transition of frequency  $\nu_0 \simeq 1901 \text{ GHz}$  the result is an emission feature in the CMB spectrum at  $\nu_{\text{obs}} = \nu_0/(1+z)$ . In the case of a receding C II ion, the opposite situation occurs, resulting into an absorption feature. C II ions in the IGM and CGM are therefore expected to generate CMB spectral distortions whose intensity depends on both their abundance and peculiar velocity, the latter being of the order of  $\sim 50 \text{ km s}^{-1}$ .

The differential amplitude  $\Delta I_{\nu}$  of the signal with respect to the CMB intensity  $I_{\nu}$  is given by (Maoli et al. 1996):

$$\Delta I_{\nu}/I_{\nu} = (1 - e^{-\tau_{\nu}}) (3 - \alpha_{\nu})(v_p/c) \quad (3)$$

where  $\alpha_{\nu} = \nu(dI_{\nu}/d\nu)/I_{\nu}$  is the CMB spectral index and the optical depth ( $\tau_{\nu}$ ) can be written as (e.g. Gallerani et al. 2006; Pallottini et al. 2014b):

$$\tau_{\nu} = f_{\nu_0} (\pi e^2 / m_e \nu_0) N_{\text{CII}} \psi, \quad (4)$$

where  $f_{\nu_0}$  is the oscillator strength of the [C II] transition (e.g. Basu et al. 2004),  $e$  and  $m_e$  are the electron charge and mass,  $N_{\text{CII}}$  is the [C II] column density<sup>5</sup>,  $\psi = \psi((\nu - \nu_0)/\Delta\nu_D)$  is the normalized line profile (e.g. Meiksin 2009),  $\Delta\nu_D = (\nu_0/c)\sqrt{2k_B T_k/m_C}$  is the thermal Doppler

broadening,  $k_B$  the Boltzmann constant,  $m_C$  the carbon atom mass, and  $c$  the speed of light. We specify that we are focusing on CMB fluctuations produced by C II ions, but the same formalism can be extended to other fine structure lines.

In Fig. 2 we show an example of [C II]-induced CMB distortions/fluctuations<sup>6</sup> for a single line of sight (l.o.s.) extracted from a simulation snapshot centered at  $z = 6$ . In the left panel we plot  $\Delta I_{\nu}/I_{\nu}$  as a function of frequency ( $\nu$ , lower axis) and velocity ( $v$ , upper axis); in the right panel, the metal patch responsible for the fluctuations is depicted by plotting the relevant physical characteristics (from top to bottom  $\Delta$ ,  $Z$  and  $v_p$ ) as a function of comoving distance ( $\text{kpc } h^{-1}$ ) along the simulated l.o.s.. The origins of the velocity (left panel) and distance (right panel) axis are shifted for displaying purpose.

Absorption ( $\Delta I_{\nu}/I_{\nu} < 0$ ) and emission ( $\Delta I_{\nu}/I_{\nu} > 0$ ) features are highlighted with a filled red and blue region, respectively. At  $\nu \simeq 271.78 \text{ GHz}$  we can see a single absorption peak (labelled  $A_1$  in the Figure); the emission is instead characterized by a double peaked structure:  $E_1$  at  $\nu \simeq 271.81 \text{ GHz}$  and  $E_2$  at  $\nu \simeq 271.85 \text{ GHz}$ . Both  $A_1$  and  $E_1$  have FWHMs of order  $\simeq 20 \text{ km s}^{-1}$ , while the FWHM of  $E_2$  is larger,  $\simeq 40 \text{ km s}^{-1}$ . The l.o.s. intersects the metal patch for  $\simeq 0.2 \text{ Mpc } h^{-1}$ . The CMB interacts with a CGM peak ( $\Delta \simeq 10^2$ ) at  $x \simeq -30 \text{ kpc } h^{-1}$  and an IGM peak ( $\Delta \simeq 10^{0.5}$ ) at  $x \simeq +75 \text{ kpc } h^{-1}$ .

The CGM is responsible for both the absorption  $A_1$  and the emission  $E_1$  features. The change from absorption to emission is caused by the change of sign in  $v_p$ . As  $N_{\text{CII}} \propto Z\Delta$ , the maximum of the CGM signal is produced rightwards of the  $\Delta$  maximum, i.e. at  $x \simeq -5 \text{ kpc } h^{-1}$ . At this location  $v_p < 0$ , thus the CGM absorption feature ( $A_1$ ) is stronger than the emission ( $E_1$ ). The broader emission peak  $E_2$  is caused by the IGM. Because of the lower density, this emission is one order of magnitude lower than the CGM absorption, and of the same order of the emission  $E_1$ .

The cumulative effect of the patch can be calculated by integrating over the shown bandwidth ( $\Delta\nu = 1 \text{ GHz}$ ). This yields a net absorption, with intensity  $\Delta I/I \simeq -7 \times 10^{-7}$ . The order of magnitude of the cumulative effect is comparable with that of the amplitude of the fluctuations due to up-scattering of CMB photons with hot electrons ( $T > 10^4 \text{ K}$ ) produced by first stars/galaxies radiation, supernova feedback and structure formation shocks at redshifts  $z > 10-20$  (e.g. Chluba 2014).

### 3 CMB FLUCTUATIONS MAPS

We select a sample of  $\simeq 4 \times 10^6$  l.o.s. extracted from a snapshot of the simulation at  $z = 6$  to compute maps of CMB metal fluctuations. At this redshift, the P14 simulation is characterized by a maximum field of view (FOV) of  $\simeq (350'')^2$  and an adaptive spatial resolution down to  $\simeq 500 \text{ pc}$ ,

<sup>4</sup> Gong et al. (2012) have shown that the IGM/CGM spin temperature of the [C II] transition is close to the CMB temperature up to  $z \simeq 2$ . At lower  $z$ , the soft UV background pumping effect may be sufficiently strong to decouple the spin temperature from the CMB temperature. Note that the redshift of the decoupling depend on the considered transition (e.g. Hernández-Monteagudo et al. 2007, for [O I]).

<sup>5</sup> Note within our formalism the ISM does not contribute to  $\tau_{\nu}$  in eq. 4, since ISM emission is accounted via the V15 model (see Sec. 2.2).

<sup>6</sup> In the CMB terminology, *distortions* indicate spectral variations, while *anisotropies* refer to spatial variations. In this work we study spectral distortions that are induced by a non-uniform distribution of metals. Throughout the paper, we refer to them as *fluctuations*.

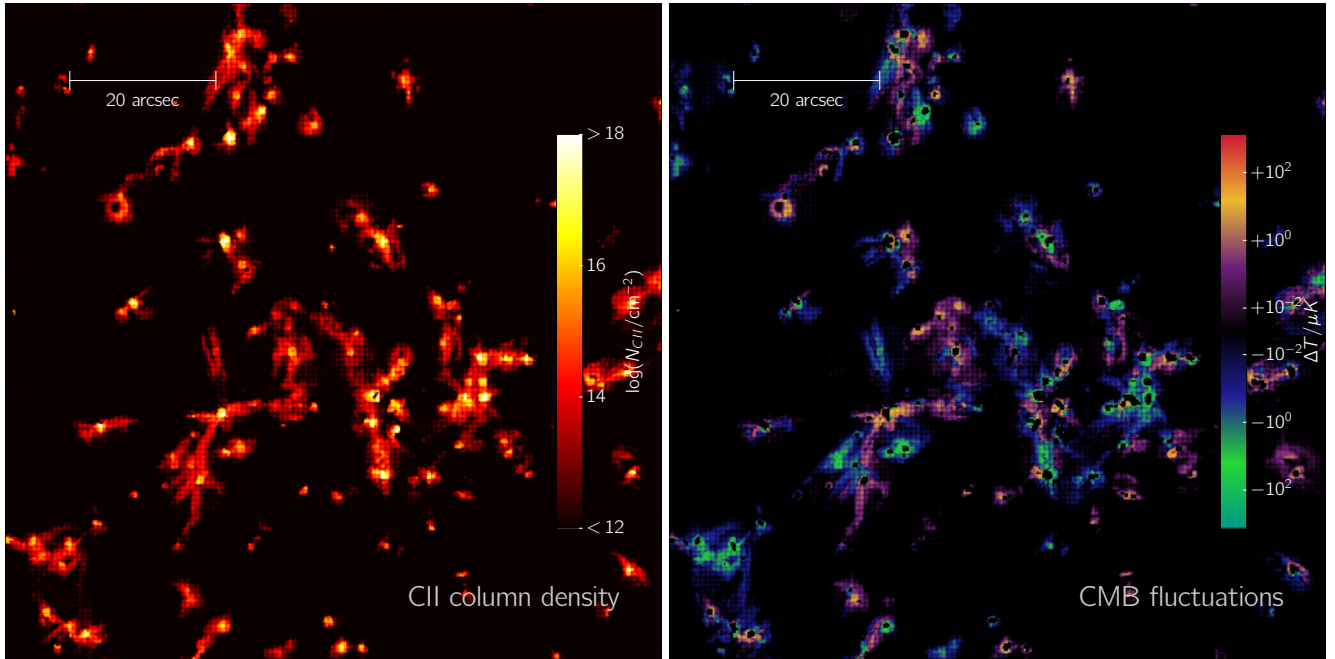


**Figure 3.** [C II] column density map (left panel) and corresponding CMB fluctuations map (right panel) from a simulated field of view (FOV) of  $\simeq (90'')^2$  at  $z = 6$ . **Left panel:** map of the [C II] column density ( $N_{\text{CII}}$ ) responsible for the CMB fluctuations. The column density is shown for the range  $12 < \log(N_{\text{CII}}/\text{cm}^{-2}) < 18$  for displaying purposes. **Right panel:** the [C II] CMB fluctuations map is shown as the brightness temperature  $\Delta T \equiv \Delta I c^2 / (2\nu^2 k_B)$  integrated on the simulation maximum available bandwidth, i.e.  $\Delta\nu \simeq 2.6$  GHz. Note that the black spots inside the fluctuation patches ( $|\Delta T| > 0$ ) are caused by the ISM masking. In both panels, the angular scale is indicated as an inset.

implying that maps are resolved at angular scales of  $\theta_{\text{res}} \simeq 0.2''$ .

Fig. 3 shows the [C II] column density map (left panel) and the corresponding CMB fluctuation map (right panel) for a FOV  $\simeq (90'')^2$ . The [C II] column densities are due to projection of the metal bubbles that originate around galaxies, pollute the IGM/CGM and extend in the cosmic web filaments. The density profiles around galaxies are self-similar once scaled with the virial radius of the parent dark matter halo (Pallottini et al. 2014b), and metals usually extend out to  $\simeq 10 r_{\text{vir}}$ . Thus, extended patches with high  $N_{\text{CII}}$  values are found nearby older (more massive) galaxies, which have more time to increase the metallicity of the central CGM part and pollute the surrounding IGM environment. As a reference, the ISM typically has  $\log(N_{\text{CII}}/\text{cm}^{-2}) \gtrsim 18$ , the CGM (IGM) can be enriched up to  $\log(N_{\text{CII}}/\text{cm}^{-2}) \gtrsim 16$  ( $\log(N_{\text{CII}}/\text{cm}^{-2}) \gtrsim 12$ ).

In the right panel of Fig. 3, CMB fluctuations are expressed in terms of differential brightness temperature,  $\Delta T \equiv \Delta I c^2 / (2\nu^2 k_B)$ , where  $\Delta I$  is obtained by integrating  $\Delta I_\nu$  (see eq. 3) on the total bandwidth of the simulation, i.e.  $\Delta\nu \simeq 2.6$  GHz. The signal ranges from emissions up to  $\Delta T \simeq +10^2 \mu\text{K}$  down to absorptions of order  $\Delta T \simeq -10^2 \mu\text{K}$ . The signal is negligible ( $|\Delta T| \lesssim 10^{-3} \mu\text{K}$ ) in  $\simeq 60\%$  of the selected FOV, consistently with the analysis of the metal filling factor at this redshift (Pallottini et al. 2014a).

The morphology of CMB fluctuations follows the  $N_{\text{CII}}$  distribution. The lack of an exact match between the respective maps is due to the dependence of  $\Delta T$  from the peculiar velocity field. Absorption and emission features can arise from the differential velocity structure inside a single metal

bubble. This is the spatial analog of the emission/absorption features as a function of  $\nu$  for the l.o.s. shown in Fig. 2.

Fluctuations are preferentially located in correspondence of  $\log(N_{\text{CII}}/\text{cm}^{-2}) > 12$  patches, characterized by typical sizes  $\theta \simeq 20''$ ; local maxima of the fluctuations ( $|\Delta T| > 10^2 \mu\text{K}$ ) are usually found in smaller spots ( $\theta \simeq 1''$ ) characterized by  $\log(N_{\text{CII}}/\text{cm}^{-2}) \simeq 17$ . This result is confirmed through the analysis of the CMB fluctuations power spectrum that peaks at angular scale  $\theta \simeq 1''$ , as detailed in App. A.

CMB fluctuations on large ( $\simeq 10''$ ) and small ( $\simeq 1''$ ) scales arise from the enriched IGM and CGM, respectively. Smaller scales correspond to the ISM of galaxies. These regions have been masked<sup>7</sup>, since they do not contribute to CMB fluctuations, while possibly shining as [C II] emitters.

The [C II] is a biased tracer of the cosmic web as it is mostly concentrated in the intersection of the filaments (“knots” hosting galactic environments) where the density is sufficiently large ( $\Delta \gtrsim 10^2$ ) that recombinations overcome photoionization from the UV background (and possibly local) radiation field. In addition, as several observational and theoretical works have shown, the filling factor of metals at these high- $z$  is relatively small, of the order of 10%-20%. So independently of the ionization state, it would be anyway difficult to find carbon in regions of moderate to low density ( $\Delta \lesssim 5$ ) corresponding to the filaments.

<sup>7</sup> The ISM masking interests less than 0.5% of the total FOV.

#### 4 MOCK OBSERVATIONS

Starting from our model for [C II]-induced CMB fluctuations and [C II] emission from  $z = 6$  galaxies, we generate mock observations specifically suited for comparison with ALMA data. The [C II] line at  $157.74 \mu\text{m}$  from  $z = 6$  is redshifted in ALMA BAND6 ( $1.1 - 1.4 \text{ mm}$ ). At this wavelength the FOV (primary beam) of ALMA antennas is  $\simeq 20''$ , and the angular resolution (synthesized beam) ranges from  $1.8''$  to  $0.14''$ , for the most compact and the most extended configuration, respectively (e.g. Maiolino 2008)<sup>8</sup>.

We account for ALMA angular resolution by convolving our maps with the synthesized beam, that can be characterized as a 2D-Gaussian. In this Sec., we assume a major axis of  $1.4''$ , a minor axis of  $0.9''$ , and a position angle of  $91.6^\circ$ .

We note that the synthesized beam that optimizes the intensity of the signal depends on the experiment that one would like to carry on. In the case of CMB fluctuations, the synthesized beam that optimizes the chance of detection is  $\simeq 1''$ , since the power spectrum peaks at this scale, as shown in Sec. 3 and by the power spectrum analysis, reported in the App A. Viceversa, for detecting [C II] emission from galaxies, a synthesized beam of  $\sim 0.5''$  is more appropriate since it corresponds to typical galaxy sizes at  $z \simeq 6$ , thus minimizing the surface-brightness bias for galaxy detection (e.g. Grazian et al. 2011). This different observational set-up is further described in Sec. 5.

CMB fluctuations and galaxy emission maps are generated by integrating on  $\Delta\nu = 8 \text{ GHz}$ , i.e. the maximum bandwidth available for continuum observations. This is done in order to maximize both the sensitivity and the possibility of finding CMB signal in the selected FOV. The P14 simulation size limits the maximum available bandwidth to  $\Delta\nu = 2.6 \text{ GHz}$  (see Sec. 3). We generate a longer light-cone by replicating the  $z = 6$  simulation box. To avoid spurious periodicity effects, we randomize the simulation box by applying translations, rotations and reflections (e.g. Blaizot et al. 2005). Then, the signal from the light-cone is integrated over  $\Delta\nu = 8 \text{ GHz}$ , by taking into account that ALMA continuum band is not contiguous, i.e. it is composed of two 4 GHz bands, separated by 10 GHz.

Finally, mock maps are combined with noise maps generated with ALMAOST (Heywood et al. 2011). Within the primary beam, the noise map has a Gaussian distribution with zero mean and r.m.s.  $\sigma_N$ ; the r.m.s. accounts for instrumental uncertainties and atmospheric conditions. We assume  $0.913 \text{ mm}$  of water vapor for our fiducial observational setting. Using the ALMA full array, we have a continuum sensitivity of  $\sigma_N \simeq 11.09 (t/\text{hr})^{-1/2} (\Delta\nu/8 \text{ GHz})^{-1/2} [\mu\text{Jy}/\text{beam}]$  for an observational time  $t$  at  $\nu_{\text{obs}} \simeq 271 \text{ GHz}$ .

In Fig. 4 we plot mock maps centered on the same  $M_{\text{UV}} \simeq -19$  galaxy. In the upper panels, we plot separately the galaxy emission (left) and CMB fluctuations (right) signals, expressed in  $\mu\text{Jy}/\text{beam}$ . The angular scale and the synthesized beam are indicated in the inset. In the galaxy emission map, the symbol ‘X’ indicates locations of galaxies, which are labelled according to their  $M_{\text{UV}}$ . Galaxies are mostly found clustered in the upper region, and the plot

shows a clear correlation between galaxy UV magnitude and [C II] emission (see the right panel of Fig. 1 in Sec. 2.2). In fact, brighter [C II] emitters ( $\Delta I \simeq \mu\text{Jy}/\text{beam}$ ) correspond to brighter UV galaxies ( $M_{\text{UV}} \simeq -19$ ), characterized by a total [C II] flux of the order of  $\Delta I \simeq 100 \mu\text{Jy}$ ; dimmer galaxies ( $M_{\text{UV}} \simeq -16.5$ ) are identified through [C II] emission peaks of the order of  $\Delta I \simeq 10^{-1} \mu\text{Jy}/\text{beam}$ ; the faintest galaxies in the map ( $M_{\text{UV}} \simeq -15$ ) show very low [C II] emission,  $\Delta I \lesssim 10^{-2} \mu\text{Jy}/\text{beam}$ .

The CMB fluctuations map (upper left panel of Fig. 4) shows various peaks both in absorption and emission. The signal due to CMB fluctuations result to be more extended and offset with respect to galaxy emission (indicated as ‘X’). This is expected from our analysis of  $N_{\text{CII}}$  and CMB fluctuations maps (see Fig. 3). Typically, emission/absorption features range between  $10^{-2} \lesssim |\Delta I|/(\mu\text{Jy}/\text{beam}) \lesssim 10^{-1}$ , with local intensity maxima comparable to the emission signal of a  $M_{\text{UV}} \simeq -17$  galaxy. The strongest peak occurs in absorption and it is characterized by  $\Delta I \lesssim -10^{-1} \mu\text{Jy}/\text{beam}$ .

In the lower panels of Fig. 4, we plot the total signal, i.e. including the contribution from CMB fluctuations, galactic emission and two different noise levels:  $\sigma_N \simeq 0.1 \mu\text{Jy}/\text{beam}$  (left) and  $\sigma_N \simeq 0.02 \mu\text{Jy}/\text{beam}$  (right) that correspond to  $t \simeq 1.3 \times 10^4 \text{ hr}$  and  $t \simeq 3.1 \times 10^5 \text{ hr}$  observing time, respectively. In these panels, the intensity of the signal is rescaled to the noise r.m.s.; additionally, detections of CMB fluctuations and galaxy emission are indicated with  $C_i$  and  $G_i$ , respectively.

For  $\sigma_N \simeq 0.1 \mu\text{Jy}/\text{beam}$ , the noise covers most of the CMB fluctuations and all the faint peaks of the galactic emission map ( $M_{\text{UV}} \gtrsim -17$ ). Detectable signals arise from the two  $M_{\text{UV}} \simeq -19$  galaxies ( $G_1$  and  $G_2$ ) and from the peak of the CMB fluctuations ( $C_1$ ); the galaxies show  $> 10\sigma_N$  emission peaks, and the fluctuation appears as a  $\simeq 7\sigma_N$  absorption signal.

In the case of the deeper mock observation, for  $\sigma_N \simeq 0.02 \mu\text{Jy}/\text{beam}$ ,  $M_{\text{UV}} \simeq -17.6$  galaxies are detectable ( $G_3$  and  $G_4$ ) at  $> 6\sigma_N$  as [C II] emitters within the primary beam. Note that  $G_3$  is a  $> 10\sigma_N$  peak, while  $G_4$  show an emission  $\simeq 6\sigma_N$ , as its signal is partially suppressed by the nearby absorption from CMB fluctuations at  $C_1$ . Three more CMB fluctuations peaks are visible on the map: a  $\simeq 6\sigma_N$  absorption arising outside the primary beam ( $C_2$ ), and two extended  $\simeq 5\sigma_N$  emissions ( $C_3$  and  $C_4$ ) located within  $2.5''$  from the  $M_{\text{UV}} \simeq -19$  galaxies.

Note that CMB fluctuations in emission can be mistaken for signals arising from galaxies. In principle, the origin of the signal can be distinguished by analyzing its spectral properties. Typically, galaxy [C II] emission lines have FWHMs  $\gtrsim 50 - 100 \text{ km s}^{-1}$  (e.g. Vallini et al. 2013; Decarli et al. 2014; Cormier et al. 2015), while CMB fluctuations usually show a double-peak structure in the spectra (see Sec. 2.3, in particular Fig. 2), with narrower lines (FWHM  $\simeq 30 - 40 \text{ km s}^{-1}$ ) both in absorption and emission.

A more robust discriminant for the nature of the signal can be provided by multiwavelength analysis. By comparing the [C II] map with UV imaging of the field, we can distinguish between the emission from CMB fluctuations and galaxies. Knowing the location and UV luminosity of galaxies in the field, we can infer the expected [C II] flux (see Sec. 2.2, in particular right panel of Fig. 1). JWST will have a

<sup>8</sup> For further details, please refer to the ALMA handbook [https://almascience.eso.org/documents-and-tools/cycle-0/alma-technical-handbook/at\\_download/file](https://almascience.eso.org/documents-and-tools/cycle-0/alma-technical-handbook/at_download/file)



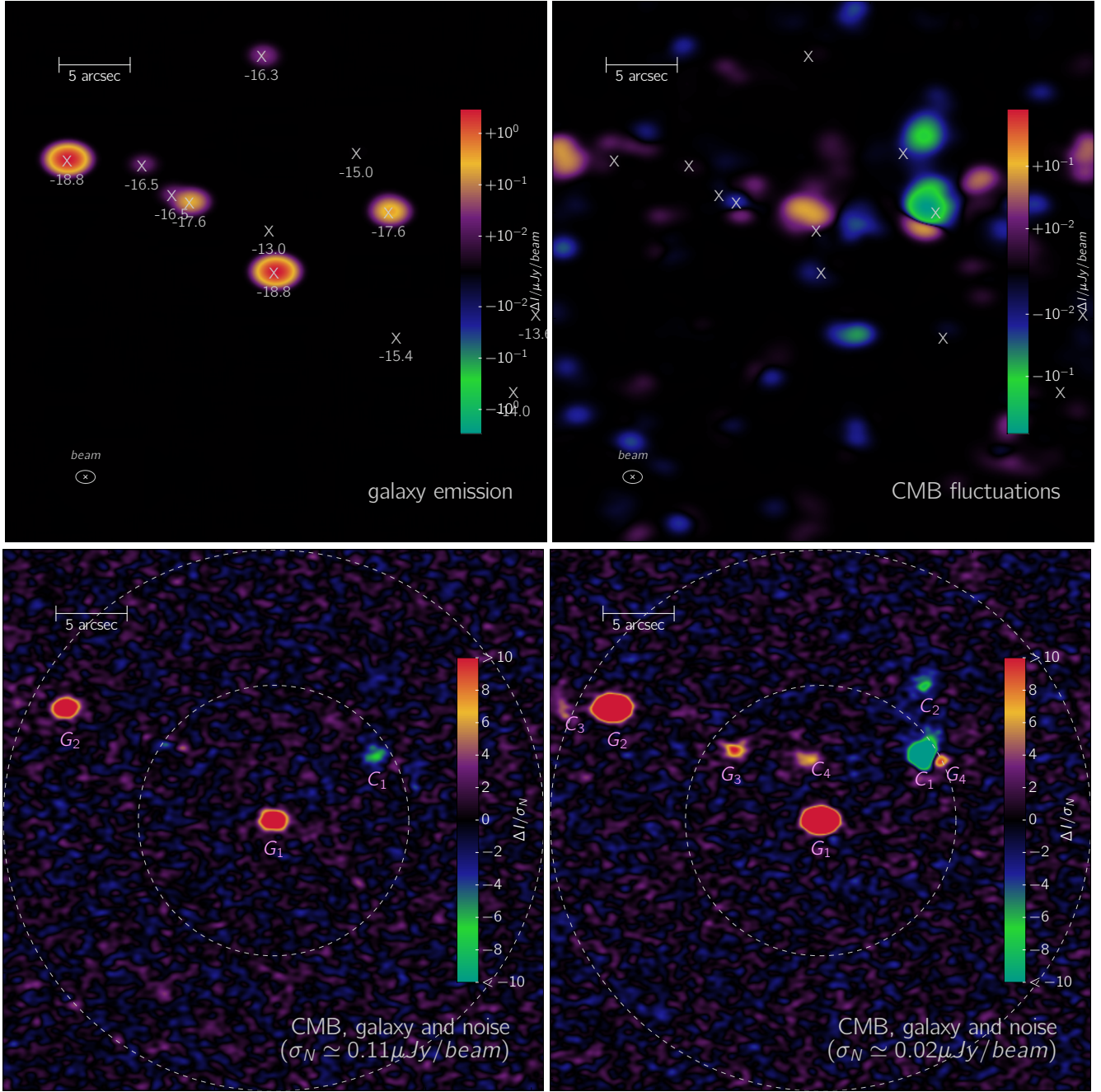


**Figure 4.** Mock ALMA [C II] continuum ( $\Delta\nu = 8$  GHz) map observed with BAND6 with a synthesized beam of  $\simeq (1'')^2$ . The maps are shown for a total FOV of  $(38.04 \simeq as)^2$ , twice BAND6 primary beam. In each panel, the map, the angular scale and the synthesized beam are indicated as insets. In the upper panels we separately plot the contribution for galaxy emission and CMB fluctuations from the same field of view. **Upper left panel:** [C II] signal from galaxy emission. The positions of galaxies are indicated with an ‘X’ and labelled with the corresponding UV magnitude ( $M_{UV}$ , details in the text). The intensity is expressed as  $\mu\text{Jy}/\text{beam}$  and, to better appreciate the presence/absence of the signal, the intensity is in symmetric logarithmic scale. **Upper right panel:** [C II] signal from CMB fluctuations from the same field of view. As for emission from galactic ISM, the intensity scale is nonlinear. **Lower left panel:** mock observation, obtained by summing the contributions from CMB fluctuation, galaxy emission and noise. The noise distributions fit a Gaussian with r.m.s.  $\sigma_N \simeq 0.11 \mu\text{Jy}/\text{beam}$ . To augment the readability of the map, the intensity is rescaled with  $\sigma_N$  and the scale is limited to  $|\Delta I| < 10 \sigma_N$ . To help the description in the text, detections of CMB fluctuations and galaxy emission are indicated with  $C_i$  and  $G_i$ , respectively. For reference, we plot the ALMA primary beam and twice the primary beam with dashed lines. **Lower right panel:** as in the lower left panel but with  $\sigma_N \simeq 0.02 \mu\text{Jy}/\text{beam}$ .



reference limiting magnitude of  $M_{\text{UV}} \simeq -16$  at  $z = 6$ , thus it seems to be perfectly suited for such comparison.

## 5 OBSERVATIONAL PROSPECTS

The amplitude of [C II]-induced CMB fluctuations is expected to be  $|\Delta I| \lesssim 1 \mu\text{Jy}/\text{beam}$ , as discussed in the previous section. With the aim of defining the optimal observational strategy for detecting such weak signals, we first consider the feasibility of a blind survey experiment with ALMA. We compute the probability distribution functions (PDFs) of the intensity of [C II]-induced CMB fluctuations and [C II] galaxy emission at  $z = 6$ . We consider the signals extracted from the whole simulation FOV,  $\simeq (350'')^2$ , on the  $\Delta\nu \simeq 2.6$  GHz bandwidth centered at the frequency  $\nu_{\text{obs}} \simeq 271$  GHz. For both signals, the intensity accounts for the  $\simeq (1'')^2$  ALMA synthesized beam introduced in Sec. 4. For each PDF, the corresponding integral is normalized to unity.

In the left panel of Fig. 5, we plot the PDFs for CMB fluctuations and galaxy emission with blue solid and red dashed lines, respectively. The plot is cut at  $|\Delta I| = 10^{-3} \mu\text{Jy}/\text{beam}$  for displaying purpose. As a reference, with vertical lines we plot  $1\text{-}\sigma$  flux detection limits that correspond to the ALMA observing time indicated in the legend, calculated with the ALMA Sensitivity Calculator<sup>9</sup>. For the CMB fluctuations, the PDF rapidly decreases from  $10^{-1.5}$  at  $|\Delta I| \simeq 10^{-3} \mu\text{Jy}/\text{beam}$  down to  $10^{-4}$  at  $|\Delta I| \simeq 10^{-0.5} \mu\text{Jy}/\text{beam}$ . For the galaxy emission, the PDF decrease is less steep, and the two PDFs cross at  $|\Delta I| \simeq 10^{-1} \mu\text{Jy}/\text{beam}$ .

We indicate with  $\sigma_N$  the  $1\text{-}\sigma$  flux detection limit of the ALMA blind survey. Then the integral of the PDF above  $\sigma_N$  provides the probability  $P_{\text{dis}}$  and  $P_{\text{gal}}$  of detecting CMB fluctuations and galaxy emission, respectively. For  $\sigma_N = 10^{-3} \mu\text{Jy}/\text{beam}$  (corresponding to an ALMA observing time  $t \simeq 10^6$  hr), we find  $P_{\text{dis}} \simeq 4\%$  and  $P_{\text{gal}} \simeq 1\%$ . Given the current telescope sensitivity, if we consider a more realistic – though challenging – observation, i.e.  $\sigma_N = 10^{-1} \mu\text{Jy}/\text{beam}$  ( $t \simeq 10^4$  hr), we find  $P_{\text{gal}} \simeq P_{\text{dis}} \simeq 0.05\%$ . This highlights that it is extremely difficult to detect CMB fluctuations with a blind survey.

Therefore, as an alternative strategy we consider the search for CMB fluctuations in the close proximity of high- $z$  galaxies. We compute the cross-correlation ( $\xi$ ) between CMB fluctuations peaks and UV galaxy emission. We calculate  $\xi$  by using an extension of the Hamilton estimator (e.g. Nollenberg & Williams 2005):

$$\xi(\theta) + 1 = (D_G D_C \langle D_R D_R \rangle) / (\langle D_G D_R \rangle \langle D_C D_R \rangle), \quad (5)$$

where  $D_i D_j$  is the number of data pairs from sets  $i$  and  $j$  within angular distance  $\theta$ , the subscripts  $G$  and  $C$  indicate the set of positions for galaxy and CMB fluctuations peaks respectively, and  $R$  labels a set of locations extracted from a random uniform distribution; the operator  $\langle \dots \rangle$  indicates the average on different realizations of  $R$ . Both the dimension of the set  $R$  and the number of realizations for the average are fixed to reach a suitable convergence for  $\xi$ .

For what concerns CMB fluctuations, we consider only strong peaks, i.e. fluctuations with  $|\Delta I| > 0.1 \mu\text{Jy}/\text{beam}$ . Within the simulated FOV we find  $\simeq 30$  of such peaks, with signal intensity up to  $0.25 \mu\text{Jy}/\text{beam}$  in emission and down to  $-0.82 \mu\text{Jy}/\text{beam}$  in absorption. For these signals, the mean  $|\Delta I|$  is  $\simeq 0.23 \mu\text{Jy}/\text{beam}$  and the r.m.s. is  $\simeq 0.25 \mu\text{Jy}/\text{beam}$ . For what concerns galaxies, we select sets of objects characterized by different UV limiting magnitudes.

In the right panel of Fig. 5, we plot with red, blue and black lines the cross-correlation calculated for galaxies with  $M_{\text{UV}} < -18$ ,  $-16$  and  $-14$ , respectively. Although there is a clear cross-correlation between strong CMB fluctuations and galaxy emission, we find no strong dependence of the correlation scale from the considered  $M_{\text{UV}}$  limits<sup>10</sup>. Therefore, the most promising – though challenging – observational strategy for detecting [C II]-induced CMB fluctuations is to perform a deep ( $\sigma_N \lesssim 0.1 \mu\text{Jy}/\text{beam}$ ) ALMA BAND6 observation pointing at a  $M_{\text{UV}} \simeq -19$  known galaxy, e.g. in the HDF south, where the deepest photometry is available. This observational strategy is detailed in Sec. 4.

From Fig. 5 it appears that [C II] emission detection is very challenging even from the bright end galaxies in our simulation ( $M_{\text{UV}} \gtrsim -19$ ). As anticipated in Sec. 4, this is critically dependent on the assumed  $\simeq 1''$  synthesized beam. A galaxy at  $M_{\text{UV}} \simeq -19$  has a [C II] emission of  $\simeq 100 \mu\text{Jy}$  (see Fig. 1 and eq. 2). This correspond to a flux of  $\simeq 1 \mu\text{Jy}/\text{beam}$  in the ALMA map with a  $\simeq 1''$  synthesized beam. Hence, with this set-up,  $\simeq 10^3$  hours of integration time are required in order to detect the signal at  $\simeq 4\sigma$ .

The detectability drastically improves when using instead a synthesized beam similar to the galaxy size, i.e.  $\simeq 0.5''$ , like the one used in recent high- $z$  observations (Maiolino et al. 2015; Capak et al. 2015; Willott et al. 2015). With this set-up, by using eq. 2 and the ALMA Sensitivity Calculator, we find that a  $M_{\text{UV}} = -18$ ,  $-19$ ,  $-20$  galaxy can be detected at  $4\sigma$  in  $\simeq 2000$ ,  $40$ ,  $1$  hours, respectively. Indeed, [C II] has been detected in high- $z$  galaxies with magnitudes up to  $M_{\text{UV}} > -20$  with  $t \sim 1$  hr (Maiolino et al. 2015; Willott et al. 2015). With a more demanding observational time of  $\sim 40$  hr, we would be able to detect  $M_{\text{UV}} \simeq -19$  galaxies at  $z \simeq 6$ , thus sampling galaxies more similar to the true reionization sources.

As noted in Pallottini et al. (2015), at  $z = 6$  P14 galaxies have a specific SFR of  $\text{sSFR} = \text{SFR}/M_* \simeq 2.5 \text{ Gyr}^{-1}$ , that is consistent with observations by Daddi et al. (2007) and González et al. (2011). However, more recent observations seem to favor an higher sSFR (e.g. Stark et al. 2013,  $\text{sSFR} = 5 \text{ Gyr}^{-1}$ ). The latter sSFR would yield a [C II] emission higher by a factor  $\simeq 2$ , namely a required observing time a factor  $\simeq 0.7$  smaller. An increase of sSFR results in an increase of metal production, that may enhance the signal of CMB fluctuations by up to a factor  $\sim 2$ . However, it is difficult to quantify this enhancement, because of the complexity of the metal enrichment process.

<sup>10</sup> The cross-correlation scale does not strongly depend on the considered  $M_{\text{UV}}$  limits because of the following. Brighter (more massive) galaxies are expected to be surrounded by more extended and enriched CGM. However CMB fluctuations linearly depend on the velocity field, thus there is a lack of correspondence between high  $N_{\text{CII}}$  values and strong fluctuations (see Sec 3 for details, in particular Fig. 3).

<sup>9</sup> <https://almascience.eso.org/proposing/sensitivity-calculator>

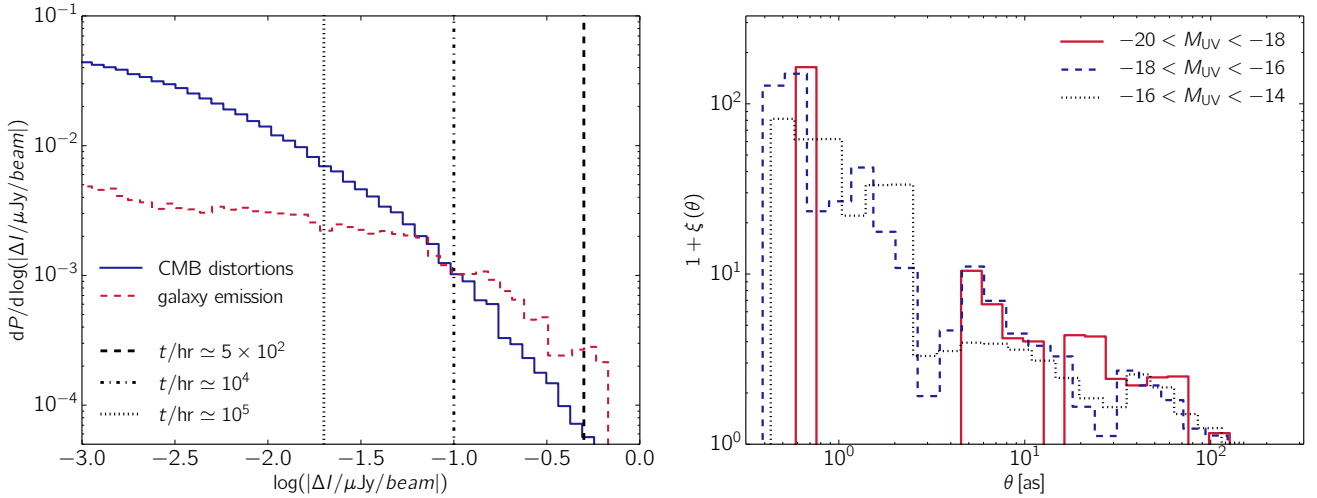


**Figure 5.** **Left panel:** PDFs of the absolute value of the signal from CMB fluctuations (blue solid line) and galaxy emission (red solid line) are plotted. Both signals account for the assumed ALMA synthesized beam (see Sec. 4). The PDF integral is normalized to unity, and the plot is cut at  $|\Delta I| = 10^{-3} \mu\text{Jy/beam}$  for displaying purpose. As a reference, with vertical lines we plot several flux detection limits: the corresponding ALMA observational time is indicated in the legend. **Right panel:** Angular cross-correlation ( $\xi$ ) function between high CMB fluctuation peaks ( $|\Delta I| > 0.1 \mu\text{Jy/beam}$ , see text) and galaxies with limiting magnitude  $M_{\text{UV}} = -18$ ,  $-16$  and  $-14$  (plotted with red, blue and black lines, respectively).

## 6 CONCLUSIONS

We have studied the possibility of mapping heavy elements via far infrared (FIR) emission from the interstellar medium (ISM) of high- $z$  galaxies and cosmic microwave background (CMB) fluctuations induced by metals in the intergalactic medium (IGM). We focus on high- $z$  low mass ( $M_\star \lesssim 10^{10} M_\odot$ ) galaxies, which are expected to be abundant at  $z \sim 6$ , and to represent the first ( $z \gtrsim 10$ ) efficient metal polluters of the IGM (e.g. Madau et al. 2001; Ferrara 2008) and sources of reionization (e.g. Barkana & Loeb 2001).

Among the FIR emission lines, the  $[\text{C II}]$  ( $^2P_{3/2} \rightarrow ^2P_{1/2}$ ) transition at  $157.74 \mu\text{m}$  is the brightest (e.g. Crawford et al. 1985; Madden et al. 1997), and it is used to trace and characterize  $z \sim 6$  galaxies (e.g. Carilli & Walter 2013). We compute both the  $[\text{C II}]$  emission arising from the ISM of  $z = 6$  galaxies and the amplitude of  $[\text{C II}]$ -induced<sup>11</sup> CMB fluctuations from metals in the IGM and circumgalactic medium (CGM).

We use state-of-the-art high- $z$  hydrodynamical simulations (Pallottini et al. 2014a) that follow the evolution of the cosmic metal enrichment from  $z = 10$  from  $z = 4$ . We calculate the galactic  $[\text{C II}]$  signal by using an ISM model (Vallini et al. 2013, 2015) that accounts for the detailed sub-kpc scales structure of the emission, namely for the cold and warm neutral medium and in high density photodissociation regions (PDRs). We calculate the CMB fluctuations induced by  $\text{C II}$  ions by modelling the resonant scattering between the CMB and metals in the IGM/CGM (e.g. Maoli et al. 1996; Basu et al. 2004) and we predict the related emission and absorption features arising in the FIR band.

We then carefully analyze the theoretical signal of CMB

fluctuations from the IGM/CGM. While the effects of resonant scattering of CMB photons by very early metals ( $z \gg 10$ ) were studied with analytical models and simple assumptions about the metal distribution (e.g. Basu et al. 2004; Schleicher et al. 2008), the present study is the first based on hydrodynamical numerical simulations extending to observable epochs ( $z \sim 6$ ). In terms of the differential brightness temperature,  $\Delta T \equiv \Delta I c^2 / (2\nu^2 k_B)$ , we calculate the signal from  $z = 6$  integrating on the simulation available bandwidth,  $\Delta\nu = 2.6 \text{ GHz}$ . We find that the metal-induced fluctuation signal is in the range  $\Delta T \simeq \pm 10^2 \mu\text{K}$ , i.e. can be seen either in emission or absorption. The peak of the signal is found on scales of  $\theta \simeq 1''$ , in correspondence of CGM absorption systems characterized by  $\text{C II}$  column density of  $\log(N_{\text{CII}}/\text{cm}^{-2}) \simeq 16$ .

To test the detectability of the  $[\text{C II}]$  signal, we have constructed and analyzed mock observations specifically suited for comparison with ALMA BAND6 data.

We predict that  $[\text{C II}]$  emission is correlated with  $M_{\text{UV}}$ . At  $M_{\text{UV}} < -20$ , the faintest high- $z$  galaxy from which  $[\text{C II}]$  emission is detected, our relation (eq. 2) is in good agreement with recent observations (Maiolino et al. 2015; Capak et al. 2015; Willott et al. 2015). We find that a  $M_{\text{UV}} = -18, -19, -20$  galaxy can be detected at  $4\sigma$  in  $\simeq 2000, 40, 1$  hours, respectively. Indeed,  $[\text{C II}]$  has been detected in high- $z$  galaxies with magnitudes up to  $M_{\text{UV}} > -20$  with  $t \sim 1 \text{ hr}$  (Maiolino et al. 2015; Willott et al. 2015). With a more demanding observational time of  $\sim 40 \text{ hr}$  at  $z \simeq 6$  we would be able to detect  $M_{\text{UV}} \simeq -19$  galaxies, thus sampling galaxies more similar to the true reionization sources. Additionally, the relation is the analogous of the local ( $z = 0$ )  $L_{\text{CII-SFR}}$  relation (De Looze et al. 2014). Eq. 2 highlights the possibility of using  $[\text{C II}]$  as a tracer of star formation activity, that can be used independently from UV flux determination. This is particularly important at high- $z$  as, contrary to UV light,  $[\text{C II}]$  emission is not affected by dust extinction.

<sup>11</sup> The presented method can be straightforwardly extended to other FIR lines, as  $[\text{N II}]$  at  $122 \mu\text{m}$ ,  $[\text{O III}]$  at  $88 \mu\text{m}$ ,  $[\text{Si I}]$  at  $129 \mu\text{m}$  and  $[\text{O I}]$  at  $63 \mu\text{m}$ .

FIR observations allow in principle to simultaneously detect galaxies and to map their surrounding CGM through [C II] induced CMB fluctuations. The detection of this signal would be a breakthrough for our understanding of the early phases of galaxy formation and cosmic enrichment. The CGM is the interface regulating the outflows of enriched material from the galaxy and the inflows of pristine gas from the IGM; it has been probed so far up to  $z \sim 2$  with absorption line experiments towards background sources, QSO or galaxies (e.g. Steidel et al. 2010; Churchill et al. 2013; Liang & Chen 2014). The intervening CGM associated with a foreground galaxy leaves an absorption feature in observed spectra. With a large number of galaxy-absorber pairs, it is then possible to statistically determine the equivalent width of a given absorption line as a function of the line of sight impact parameter. Detecting CMB fluctuations is equivalent to actually map the bidimensional distribution of metals in the CGM, and it would allow to extend the enrichment study at higher redshift.

We have compared the efficiency of different observational strategies for detecting [C II] induced CMB fluctuations. We find that this signal is very faint, e.g.  $|\Delta I| \simeq 10^{-1} \mu\text{Jy}/\text{beam}$ . Because of the signal amplitude and the [C II] emission filling factor, we find that a blind experiment yields a low probability for the signal detection. However, in our maps we see strong (i.e.  $|\Delta I| \gtrsim 10^{-1} \mu\text{Jy}/\text{beam}$ ) CMB fluctuations, that are characterized by a mean  $|\Delta I|$  of  $\simeq 0.23 \mu\text{Jy}/\text{beam}$  a r.m.s. of  $\simeq 0.25 \mu\text{Jy}/\text{beam}$  and maximum  $|\Delta I|$  up to  $0.82 \mu\text{Jy}/\text{beam}$ . On average, these fluctuations have signals comparable to the typical [C II] emission from a  $M_{\text{UV}} \simeq -18$  galaxy. Our analysis highlights that strong CMB fluctuations are found typically within  $\sim 10''$  of galaxies, regardless of their  $M_{\text{UV}}$ .

We have also considered an alternative observational strategy to detect (strong) CMB fluctuations that consists of a deep ALMA pointing in a field where known  $M_{\text{UV}} \simeq -19$  galaxies (e.g. in the HDF south) are present. Our model predicts that, for an ALMA sensitivity of  $\sigma_N = 0.1 \mu\text{Jy}/\text{beam}$  CMB fluctuations would be detected at a confidence level  $\sigma > 3, 7$  with a probability  $\simeq 25\%, 5\%$ , respectively, while for  $\sigma_N = 0.05 \mu\text{Jy}/\text{beam}$  we expect a detection of CMB fluctuations with c.l.  $\sigma > 3, 5, 7$  with a probability  $\simeq 70\%, 30\%, 15\%$ , respectively. We note that the sensitivity requested for detecting [C II] induced CMB fluctuations ( $\sigma_N \lesssim 0.1 \mu\text{Jy}/\text{beam}$ ) corresponds to extremely long ALMA observing times ( $t \gtrsim 10^4 \text{hr}$ ), making the detection of this signal extremely challenging with current facilities.

However, by stacking deep ALMA observations ( $\nu_{\text{obs}} \simeq 272 \text{GHz}$ ) of several  $M_{\text{UV}} \simeq -19$  (lensed) galaxies it may be possible to “statistically” detect such elusive CMB fluctuations induced by C II ions at  $z \simeq 6$ . The same experiment, repeated at different frequencies ( $\nu_{\text{obs}} \simeq 1900/(1+z) \text{GHz}$ ) would allow to track the metal enrichment history through cosmic times. We defer this further statistical analysis to a future study.

## ACKNOWLEDGMENTS

We thank A. Mesinger for useful discussions.

## References

- Abel N. P., 2006, *MNRAS*, **368**, 1949  
 Barkana R., Loeb A., 2001, *Phys. Rep.*, **349**, 125  
 Barnes L. A., Garel T., Kacprzak G. G., 2014, *Publ. Astr. Soc. Pac.*, **126**, 969  
 Basu K., 2007, *New Astronomy Reviews*, **51**, 431  
 Basu K., Hernández-Monteagudo C., Sunyaev R. A., 2004, *A&A*, **416**, 447  
 Becker G. D., Rauch M., Sargent W. L. W., 2009, *ApJ*, **698**, 1010  
 Behar E., Dado S., Dar A., Laor A., 2011, *ApJ*, **734**, 26  
 Bell T. A., Viti S., Williams D. A., Crawford I. A., Price R. J., 2005, *MNRAS*, **357**, 961  
 Blaizot J., Wadadekar Y., Guiderdoni B., Colombi S. T., Bertin E., Bouchet F. R., Devriendt J. E. G., Hatton S., 2005, *MNRAS*, **360**, 159  
 Bouwens R. J., et al., 2012, *ApJ*, **754**, 83  
 Bouwens R. J., et al., 2014, preprint, ([arXiv:1403.4295](https://arxiv.org/abs/1403.4295))  
 Campana S., Thöne C. C., de Ugarte Postigo A., Tagliaferri G., Moretti A., Covino S., 2010, *MNRAS*, **402**, 2429  
 Campana S., Salvaterra R., Ferrara A., Pallottini A., 2015, *A&A*, **575**, A43  
 Capak P. L., et al., 2015, preprint, ([arXiv:1503.07596](https://arxiv.org/abs/1503.07596))  
 Carilli C. L., Walter F., 2013, *ARA&A*, **51**, 105  
 Cen R., Chisari N. E., 2011, *ApJ*, **731**, 11  
 Chluba J., 2014, preprint, ([arXiv:1405.6938](https://arxiv.org/abs/1405.6938))  
 Churchill C. W., Trujillo-Gomez S., Nielsen N. M., Kacprzak G. G., 2013, *ApJ*, **779**, 87  
 Ciardi B., Ferrara A., 2005, *Space Science Reviews*, **116**, 625  
 Ciccone C., et al., 2015, *A&A*, **574**, A14  
 Cormier D., et al., 2015, preprint, ([arXiv:1502.03131](https://arxiv.org/abs/1502.03131))  
 Crawford M. K., Genzel R., Townes C. H., Watson D. M., 1985, *ApJ*, **291**, 755  
 D’Odorico V., et al., 2013, *MNRAS*, **435**, 1198  
 Daddi E., et al., 2007, *ApJ*, **670**, 156  
 Dayal P., Ferrara A., Dunlop J. S., 2013, *MNRAS*, **430**, 2891  
 Dayal P., Ferrara A., Dunlop J. S., Pacucci F., 2014, *MNRAS*, **445**, 2545  
 De Looze I., et al., 2014, *A&A*, **568**, A62  
 Decarli R., et al., 2014, *ApJL*, **782**, L17  
 Dunlop J. S., 2013, in Wiklind T., Mobasher B., Bromm V., eds, *Astrophysics and Space Science Library* Vol. 396, *Astrophysics and Space Science Library*. p. 223 ([arXiv:1205.1543](https://arxiv.org/abs/1205.1543)), doi:10.1007/978-3-642-32362-1\_5  
 Ferland G. J., Korista K. T., Verner D. A., Ferguson J. W., Kingdon J. B., Verner E. M., 1998, *Publ. Astr. Soc. Pac.*, **110**, 761  
 Ferrara A., 2008, in Hunt L. K., Madden S. C., Schneider R., eds, *IAU Symposium* Vol. 255, *IAU Symposium*. pp 86–99, doi:10.1017/S1743921308024630  
 Ferrara A., Tolstoy E., 2000, *MNRAS*, **313**, 291  
 Gallerani S., Choudhury T. R., Ferrara A., 2006, *MNRAS*, **370**, 1401  
 Gallerani S., et al., 2012, *A&A*, **543**, A114  
 Gnedin N. Y., Ostriker J. P., 1997, *ApJ*, **486**, 581  
 Gong Y., Cooray A., Silva M., Santos M. G., Bock J., Bradford C. M., Zemcov M., 2012, *ApJ*, **745**, 49  
 González-López J., et al., 2014, *ApJ*, **784**, 99  
 González V., Labbé I., Bouwens R. J., Illingworth G., Franx M., Kriek M., 2011, *ApJL*, **735**, L34  
 Grazian A., et al., 2011, *A&A*, **532**, A33  
 Haardt F., Madau P., 1996, *ApJ*, **461**, 20  
 Haardt F., Madau P., 2012, *ApJ*, **746**, 125  
 Hernández-Monteagudo C., Verde L., Jimenez R., 2006, *ApJ*, **653**, 1  
 Hernández-Monteagudo C., Haiman Z., Jimenez R., Verde L., 2007, *ApJL*, **660**, L85  
 Heywood I., Avison A., Williams C. J., 2011, preprint, ([arXiv:1106.3516](https://arxiv.org/abs/1106.3516))



Johnson J. L., Dalla V. C., Khochfar S., 2013, *MNRAS*, **428**, 1857

Larson D., et al., 2011, *ApJS*, **192**, 16

Leitherer C., Ortiz Otálvaro P. A., Bresolin F., Kudritzki R.-P., Lo Faro B., Pauldrach A. W. A., Pettini M., Rix S. A., 2010, *ApJS*, **189**, 309

Liang C. J., Chen H.-W., 2014, *MNRAS*, **445**, 2061

Madau P., Dickinson M., 2014, *ARA&A*, **52**, 415

Madau P., Ferrara A., Rees M. J., 2001, *ApJ*, **555**, 92

Madden S. C., Poglitsch A., Geis N., Stacey G. J., Townes C. H., 1997, *ApJ*, **483**, 200

Maiolino R., 2008, *New Astronomy Reviews*, **52**, 339

Maiolino R., et al., 2005, *A&A*, **440**, L51

Maiolino R., et al., 2015, preprint, ([arXiv:1502.06634](https://arxiv.org/abs/1502.06634))

Maoli R., Ferrucci V., Melchiorri F., Signore M., Tosti D., 1996, *ApJ*, **457**, 1

Maoli R., et al., 2005, in Wilson A., ed., *ESA Special Publication Vol. 577, ESA Special Publication*. pp 293–296 ([arXiv:astro-ph/0411641](https://arxiv.org/abs/astro-ph/0411641))

Meiksin A. A., 2009, *Reviews of Modern Physics*, **81**, 1405

Mesinger A., McQuinn M., Spergel D. N., 2012, *MNRAS*, **422**, 1403

Muñoz J. A., Furlanetto S. R., 2014, *MNRAS*, **438**, 2483

Nagamine K., Wolfe A. M., Hernquist L., 2006, *ApJ*, **647**, 60

Nollenberg J. G., Williams L. L. R., 2005, *ApJ*, **634**, 793

Oppenheimer B. D., Davé R., Finlator K., 2009, *MNRAS*, **396**, 729

Oppenheimer B. D., Davé R., Katz N., Kollmeier J. A., Weinberg D. H., 2012, *MNRAS*, **420**, 829

Ota K., et al., 2014, *ApJ*, **792**, 34

Pallottini A., Ferrara A., Gallerani S., Salvadori S., D’Odorico V., 2014a, *MNRAS*, **440**, 2498

Pallottini A., Gallerani S., Ferrara A., 2014b, *MNRAS*, **444**, L105

Pallottini A., et al., 2015, preprint, ([arXiv:1506.07173](https://arxiv.org/abs/1506.07173))

Planck Collaboration et al., 2013, preprint, ([arXiv:1303.5076](https://arxiv.org/abs/1303.5076))

Press W. H., Schechter P., 1974, *ApJ*, **187**, 425

Rasera Y., Teyssier R., 2006, *A&A*, **445**, 1

Ryan-Weber E. V., Pettini M., Madau P., Zych B. J., 2009, *MNRAS*, **395**, 1476

Salvadori S., Ferrara A., Schneider R., 2008, *MNRAS*, **386**, 348

Schleicher D. R. G., Galli D., Palla F., Camenzind M., Klessen R. S., Bartelmann M., Glover S. C. O., 2008, *A&A*, **490**, 521

Shull J. M., 2014, *ApJ*, **784**, 142

Simcoe R. A., et al., 2011, *ApJ*, **743**, 21

Songaila A., 2005, *AJ*, **130**, 1996

Stark D. P., Schenker M. A., Ellis R., Robertson B., McLure R., Dunlop J., 2013, *ApJ*, **763**, 129

Steidel C. C., Erb D. K., Shapley A. E., Pettini M., Reddy N., Bogosavljević M., Rudie G. C., Rakic O., 2010, *ApJ*, **717**, 289

Suginohara M., Suginohara T., Spergel D. N., 1999, *ApJ*, **512**, 547

Teyssier R., 2002, *A&A*, **385**, 337

Theuns T., Leonard A., Efstathiou G., Pearce F. R., Thomas P. A., 1998, *MNRAS*, **301**, 478

Tielens A. G. G. M., Hollenbach D., 1985, *ApJ*, **291**, 747

Tomassetti M., Porciani C., Romano-Díaz E., Ludlow A. D., 2015, *MNRAS*, **446**, 3330

Troncoso P., et al., 2014, *A&A*, **563**, A58

Vallini L., Gallerani S., Ferrara A., Baek S., 2013, *MNRAS*, **433**, 1567

Vallini L., Gallerani S., Ferrara A., Pallottini A., Yue B., 2015, preprint, ([arXiv:1507.00340](https://arxiv.org/abs/1507.00340))

Vasta M., Barlow M. J., Viti S., Yates J. A., Bell T. A., 2010, *MNRAS*, **404**, 1910

White M., Carlstrom J. E., Dragovan M., Holzapfel W. L., 1999, *ApJ*, **514**, 12

Willott C. J., Carilli C. L., Wagg J., Wang R., 2015, preprint, ([arXiv:1504.05875](https://arxiv.org/abs/1504.05875))

Wolfire M. G., Hollenbach D., McKee C. F., Tielens A. G. G. M., Bakes E. L. O., 1995, *ApJ*, **443**, 152

Wolfire M. G., McKee C. F., Hollenbach D., Tielens A. G. G. M., 2003, *ApJ*, **587**, 278

Wyithe J. S. B., Bolton J. S., 2011, *MNRAS*, **412**, 1926

Yue B., Ferrara A., Pallottini A., Gallerani S., Vallini L., 2015, *MNRAS*, **450**, 3829

Zaldarriaga M., Seljak U., 2000, *ApJS*, **129**, 431

Zheng W., et al., 2012, *Nature*, **489**, 406

da Cunha E., et al., 2013, *ApJ*, **766**, 13

de Bernardis P., et al., 1993, *A&A*, **269**, 1

This paper has been typeset from a  $\text{\LaTeX}$  file prepared by the author.

## APPENDIX A: POWER SPECTRUM

We investigate the CMB fluctuations morphology by calculating the angular power spectrum (PS,  $C_l$ ) of their amplitude. At  $z = 6$  the simulation FOV is limited to  $\simeq (350'')^2$ , therefore the minimum angular scale solved is  $l \simeq 10^4$ . This allows us to compute the  $C_l$  in the flat-sky approximation (e.g. [White et al. 1999](#); [Mesinger et al. 2012](#)). We calculate PS for different bandwidths  $20 \text{ MHz} \lesssim \Delta\nu \lesssim 2.6 \text{ GHz}$ , where the upper limit of the interval represents the total bandwidth of the simulation. For  $\Delta\nu \lesssim 1.3 \text{ GHz}$ , this procedure provides multiple bandwidths that we assume to be independent to calculate the averaged  $C_l$ .

In upper panel of Fig. A1, we plot the power spectrum as  $P_l = l(l+1)C_l/2\pi$  as a function of the angular scale ( $\theta = 2\pi/l$ ) for different bandwidths, as indicated in the legend. Independently of  $\Delta\nu$ , the power spectrum has a noise-like shape, i.e.  $P_l \propto l^2$ , for  $l \lesssim 10^6$ . In correspondence of smaller scales,  $P_l$  reaches a peak at  $\theta \simeq 1''$  and then flattens, confirming the qualitative analysis discussed in Sec. 3.

In the central panel of Fig. A1, we compare our result ( $\Delta\nu \simeq 2.6$ , solid black line) and PS for CMB distortions/fluctuations induced by primordial chemistry ([Basu 2007](#), violet dotted line). The latter PS is obtained for C II that are assumed to be uniformly distributed ( $\Delta = 1$ ) at  $z = 4$  with  $Z = 10^{-1}Z_\odot$ . With a grey shaded region we indicate the cosmic variance of the [C II]-induced CMB fluctuations. As a reference, we plot the primary CMB power spectrum inferred from *Planck* observations ([Planck Collaboration et al. 2013](#), red crosses) and calculated with CMBFAST ([Zaldarriaga & Seljak 2000](#), green dashed line).

For the primordial fluctuations,  $P_l$  has a functional dependence on  $l$  as the primary CMB power spectrum ([Basu 2007](#); [Schleicher et al. 2008](#)). With respect to the primary power spectrum, these induced fluctuations produce a  $\sim 10^4$  smaller power, e.g.  $P_l \lesssim \mu K^2$  on scales  $l \lesssim 10^3$  ([Basu et al. 2004](#); [Basu 2007](#)).

We define, the PS peak as  $\langle \Delta T \rangle = \sqrt{P_l}$  at  $\theta \simeq 1''$ , and we study its dependence on  $\Delta\nu$ . The result is shown in the lower panel of Fig. A1, where we plot the PS peak mean value (red circles), the r.m.s. variance (green pentagons) and the max/min values (blue triangles) as a function of  $\Delta\nu$ . We restate that the mean and variance are calculated for the multiple bandwidths extracted from the simulation: they must not be confused with variation of CMB fluctuations from different metal bubbles.

The peak value increases with decreasing bandwidth up to  $\Delta\nu \simeq 300 \text{ MHz}$ , and decreases for smaller  $\Delta\nu$ . This behavior can be explained as follows. The peak value increases as the bandwidth becomes comparable to metal bubble size in frequency

<sup>12</sup> As shown in [Basu \(2007\)](#), in particular, see left panel of Fig. 1), at a different redshift, the primordial chemistry PS induced by C II is comparable to the one reported here.

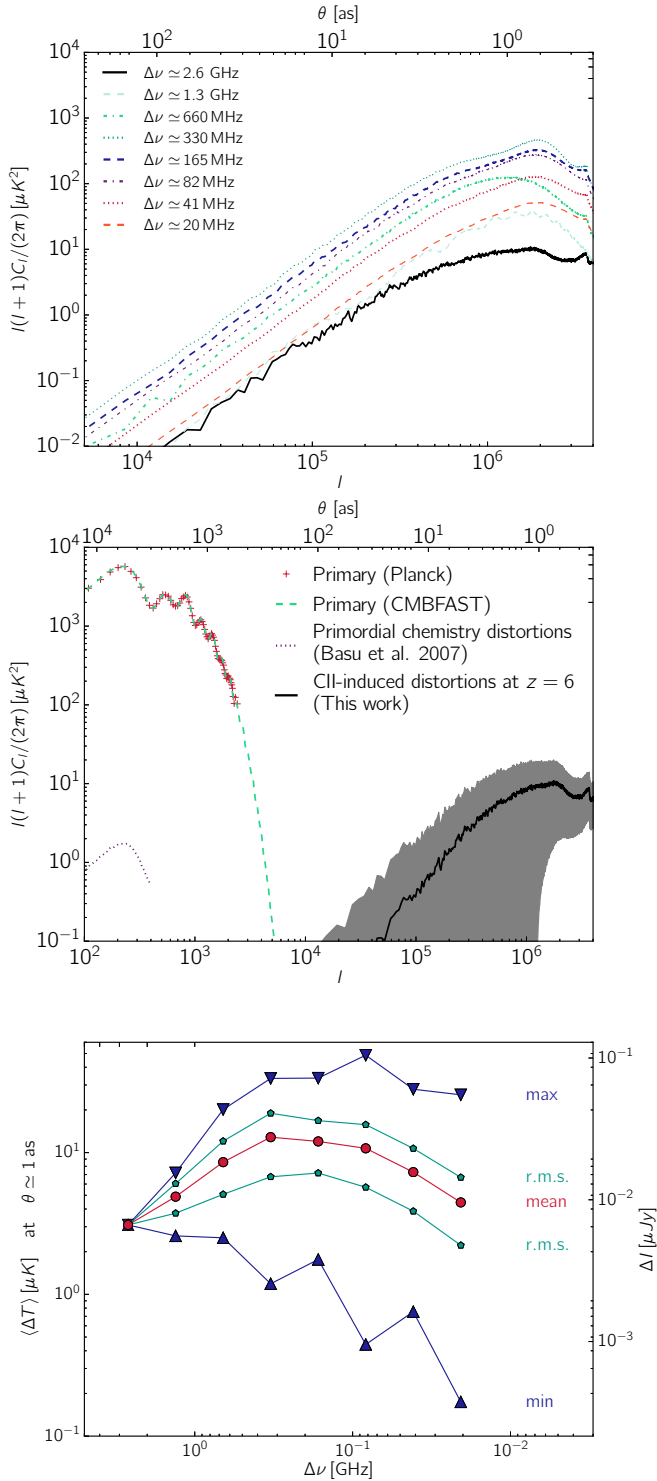


**Figure A1.** [C II]-induced CMB power spectrum (PS,  $P_l = l(l+1)C_l/2\pi$ ) as a function of the angular scale,  $l$  and  $\theta$  in the lower and upper axis, respectively. In the **upper panel** we plot  $P_l$  calculated for different bandwidths, as indicated in the legend. In the **central panel** we compare our result with other PSs, as detailed in the legend and in the text. A color version of the plot is available in the online version of the paper. **Lower panel:** maximum of PS ( $\langle\Delta T\rangle = \sqrt{P_l}$  at  $\theta \simeq 1''$ ) as a function of the bandwidth ( $\Delta\nu$ ). For each  $\Delta\nu$  we plot the mean (red circles), the r.m.s. variance (green pentagons) and the max/min values (blue triangles). The maximum is indicated in unit of  $\mu\text{K}$  (left axis) and  $\mu\text{Jy}$  (right axis).

space (see Fig. 2). As we further decrease  $\Delta\nu$ , it becomes increasingly difficult to find enriched structure in the selected bandwidth, and the peak becomes shallower.

Finally, note that the peak ( $\sqrt{P_l}$ ) increases faster than  $\Delta\nu^{-1}$  for  $2.6 \gtrsim \Delta\nu/\text{GHz} \gtrsim 0.3$  and decreases for smaller  $\Delta\nu$ . The power spectrum of a pure noise is expected to behave as  $\Delta\nu^{-1/2}$ . Therefore – in principle – the peculiar trend with  $\Delta\nu$  can discriminate a signal from CMB fluctuations from noise.